A Broadband Polarization-Insensitive Graphene Modulator Based on Dual Built-in Orthogonal Slots Plasmonic Waveguide

Wei Chen [1], Yan Xu [1], Yang Gao [1], Lanjing Ji [2], Xibin Wang [1], Xiaoqiang Sun [1,*] and Daming Zhang [1]

1   State Key Laboratory of Integrated Optoelectronics, College of Electronic Science & Engineering, Jilin University, Changchun 130012, China; chenwei18@mails.jlu.edu.cn (W.C.); xyan17@mails.jlu.edu.cn (Y.X.); ygao17@mails.jlu.edu.cn (Y.G.); xibinwang@jlu.edu.cn (X.W.); zhangdm@jlu.edu.cn (D.Z.)
2   Institute of Marine Science and Technology, Shandong University, Qingdao 250100, China; jilanting@sdu.edu.cn
*   Correspondence: sunxq@jlu.edu.cn

Abstract: A broadband polarization-insensitive graphene modulator has been proposed. The dual built-in orthogonal slots waveguide allows polarization independence for the transverse electric (TE) mode and the transverse magnetic (TM) mode. Due to the introduction of metal slots in both the vertical and horizontal directions, the optical field as well as the electro-absorption of graphene are enhanced by the plasmonic effect. The proposed electro-optic modulator shows a modulation depth of 0.474 and 0.462 dB/μm for two supported modes, respectively. An ultra-low effective index difference of 0.001 can be achieved within the wavelength range from 1100 to 1900 nm. The 3 dB-bandwidth is estimated to be 101 GHz. The power consumption is 271 fJ/bit at a modulation length of 20 μm. The proposed modulator provides high speed broadband solutions in microwave photonic systems.

Keywords: graphene; plasmonic modulator; waveguide; polarization-insensitive

1. Introduction

High performance electro-optic (EO) modulators are highly demanded in wideband optics communication networks [1]. The lithium niobite-based modulators are mature but suffer from a large footprint [2]. Silicon modulators are compatible with CMOS technology, while facing the problem of low EO efficiency [3]. III-V based modulators offer a small footprint; however, the insertion loss and thermal stability are still to be improved [4]. SiC-based waveguides also show application potential [5]. Due to the unsatisfactory EO properties of the above underlying materials, modulators that meet all requires are still elusive. Graphene with excellent EO characteristics has been well studied and widely adopted in optical modulators [6–9]. In 2011, Liu et al. experimentally presented a graphene modulator with a modulation depth (MD, the difference between "ON" state and "OFF" state) of 0.1 dB/μm [10]. A built-in p-oxide-n-like junction graphene modulator exhibited an MD of 0.16 dB/μm and a power consumption of 1 pJ/bit [11]. The graphene EO modulator with a high 3 dB-bandwidth of 30 GHz has also been demonstrated [12]. However, the performance of above graphene modulators is limited by the weak interaction between the extremely thin graphene flake and the light field that is strongly bounded in the high index dielectric material. If the plasmonic effect is introduced, the light can propagate as a surface plasmon polarizations (SPPs) mode along the waveguide, which implies an enhanced optical field intensity. More optical power will be guided to the dielectric/graphene interface, facilitating the light–graphene interaction [13–15]. Huang et al. proposed a waveguide-coupled hybrid plasmonic graphene modulator with a 3 dB-bandwidth of 0.48 THz and an energy consumption of 145 fJ/bit [16]. A hybrid plasmonic graphene modulator with a 3 dB-bandwidth of 0.662 THz and a power consumption of 118.7 fJ/bit

promises good potential for hybrid plasmonic graphene EO modulators [17]. Another issue for the graphene modulator is the polarization sensitivity, which originates from the low absorption rate of 2.3% for the electric field polarization perpendicular to the graphene flake surface. Most reported works can only operate in transverse magnetic (TM) or transverse electric (TE) polarization independently [18]. The introduction of polarization control functions will inevitably complexify the device structure [19]. Therefore, a compact and polarization-insensitive graphene modulator with characteristic of broadband operation is desirable.

In this paper, we proposed a graphene modulator based on a dual built-in orthogonal slots waveguide (DBOSW). The geometric parameters of the hybrid plasmonic waveguide are investigated and optimized by finite element method (FEM). The mechanism of polarization insensitivity and broadband modulation is elaborated in detail. Our proposed waveguide structure overcomes the strict polarization dependence of plasmonic-based waveguides. Moreover, the DBOSW graphene modulator realizes broadband modulation with excellent polarization independence, which shows good potential in microwave photonic systems.

2. Configuration and Structure

2.1. Device Structure

As shown in Figure 1, the proposed graphene modulator based on the dual built-in orthogonal slots waveguide consists of a bottom silver layer (Ag, n_{Ag} = 0.14447 + 11.366), a middle silica layer (SiO$_2$, n_{SiO2} = 1.45) and a top silver slot isolated by SiO$_2$. Double 0.33 nm-thick graphene flakes are isolated by 15 nm-thick SiO$_2$ and cover the hybrid waveguide. The metal stacks–graphene contacts form the electrodes [20]. The whole structure is supported by the SiO$_2$ substrate.
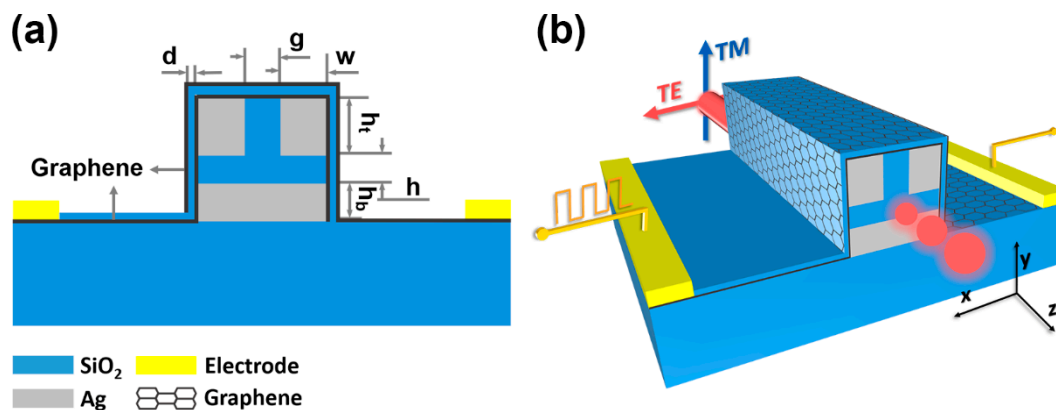

Figure 1. (**a**) Two-dimensional (2D) cross section; (**b**) three-dimensional (3D) view of the graphene modulator with dual built-in orthogonal slots waveguide.

Graphene plays a major role in optical modulation of this modulator. As shown in Figure 2a, the transmission spectrum of DBOSW with a modulation length of L = 20 μm covered with graphene-SiO$_2$-graphene stacks but without applied voltage (U = 0 V (μ_c = 0 eV)) has a sharp drop compared to DBOSW without graphene. This large significant light loss mainly originates from the light absorption effect of graphene, indicating that graphene has an effective light modulation function.
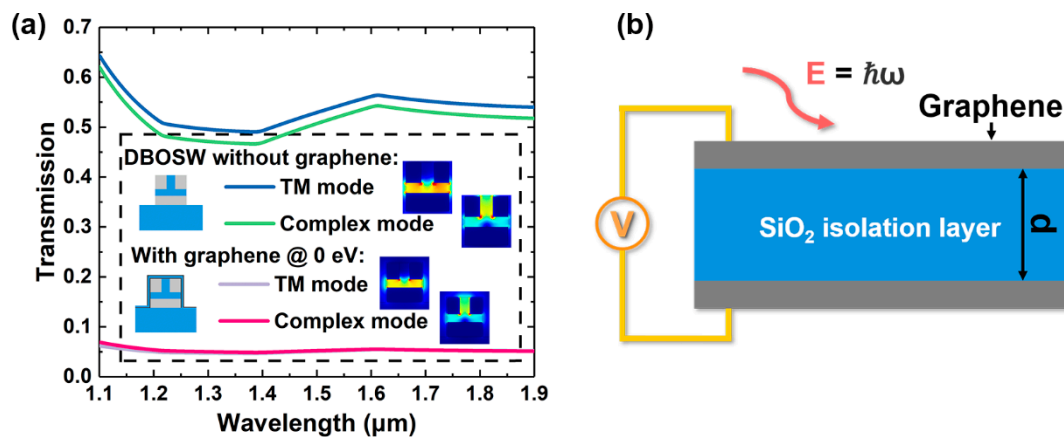
Figure 2. (**a**) Transmission spectrum of the dual built-in orthogonal slots waveguide (DBOSW) with and without graphene; (**b**) optical absorption in the graphene capacitor structure.

Two modes with different electric field polarizations are supported by the dual built-in orthogonal slots waveguide. The distributions of transversal and longitudinal electric field components of the transverse polarization (TM) mode and the complex-polarization mode (complex mode) are illustrated by $|E_x|$ and $|E_y|$, respectively. As depicted in Figure 3a, the TM mode is mainly distributed in the middle silica layer, which is attributed to the excitation of surface plasmon polarizations (SPPs) constrained by the top and bottom Ag layers. This E_y-dominated plasmonic mode is similar to the optical mode constrained in the metal slot waveguide [21]. As shown in Figure 3b, the complex mode is mainly distributed in the upper slot and extends into the middle SiO_2 layer. It should be noted that the complex mode can be seen as a mix of plasmonic modes supported by the crossed vertical metal slot and horizontal metal slot. In this case, both E_y and E_x components exist. The symmetry of both the horizontal and the vertical metal–insulator–metal (MIM) substructures lead to the spreading of transversal and longitudinal polarizations into the in-plane graphene-SiO_2-graphene layers, which is remarkably favorable to polarization-insensitive modulation.
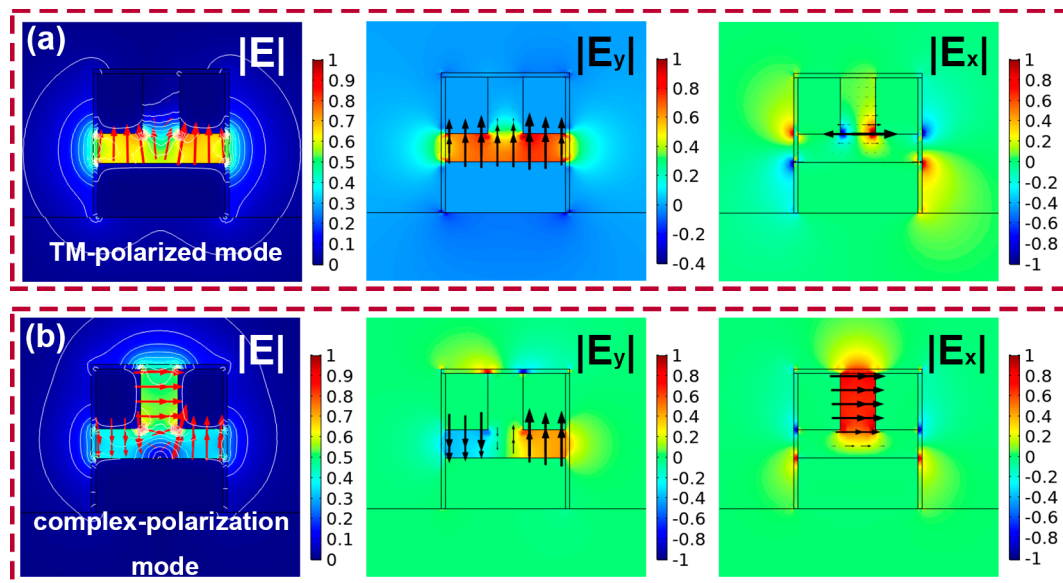

Figure 3. The electric field distributions of (**a**) transverse magnetic (TM) polarized mode and (**b**) complex-polarization mode. The color bars and arrows represent the intensity and direction of the electric field, respectively.

In order to better illustrate the waveguide optimization and characterize the modulation performance of proposed design, the mode power attenuation (MPA), modulation depth (MD) and propagation loss (PL) are defined as follows:

$$\text{MPA} = 40\pi(\log_{10}\text{e})\text{Im}(N_{\text{eff}})/\lambda \tag{1}$$

$$\text{MD} = \text{MPA}(\text{OFF}) - \text{MPA}(\text{ON}) \tag{2}$$

$$\text{PL} = \text{MPA}(\text{ON}) \tag{3}$$

where λ is the incident wavelength, $\text{Im}(N_{\text{eff}})$ is the imaginary part of the effective index, MD is defined as the difference between MPA ("ON" state) and MPA ("OFF" state) and PL refers to MPA ("ON" state).

2.2. Graphene Film

Graphene is an emerging material with single layer carbon atoms in the form of hexagons. This unique structure offers graphene optical properties of controllable light absorption, considerable carrier mobility, uniform light absorption rate of 2.3% in a broadband, etc. [10,22–30]. These favorable properties imply the graphene has good potential in the application of high-speed, low-footprint and low-power consumption devices.

As shown in Figure 2b, a plate capacitor is formed by applying bias voltage to graphene layers. Light absorption is then controlled by the applied external electric field via the electrostatic doping effect. Since the interband transition in graphene is affected by Fermi level with no consideration of sign, both graphene layers can simultaneously be "transparent" at the high driving voltage, which refers to the "ON" state. An efficient numerical calculation method is important [31]. As has been reported [32], the graphene layer can be modeled as a 3D bulk material with a constant thickness or a 2D surface structure. To obtain accurate results, a smaller grid size is required in 3D simulations, which implies longer calculation time and larger memories requirement. On the basis of accuracy, it is desirable to model graphene as a 2D layer for higher efficiency. In this work, the graphene layer is considered a surface conductivity dielectric with a thickness of zero. Benefit from the reduced number of meshes, the calculation time reduces with accuracy guaranteed. The surface conductivity σ_{g} of the graphene may be adjusted by its chemical potential μ_{c}. This process can be well described by the Kubo formula [33], in which τ corresponds to the relaxation time, the intraband transition τ_1 is 1.2 ps and the interband transition τ_2 is 15 fs. Graphene layers exhibit special physical properties at the epsilon-near-zero (ENZ) point, $\mu_{\text{c}}(\text{ENZ}) \approx 0.5$ eV [34]. When μ_{c} is larger than $\mu_{\text{c}}(\text{ENZ})$, graphene shows the characteristics of the dielectric medium. Conversely, graphene behaves like a metallic layer and strong light absorption happens when μ_{c} is smaller than $\mu_{\text{c}}(\text{ENZ})$. Equation (4) illustrates the relationship between chemical potential and bias voltage [30]:

$$\mu_{\text{c}} = \hbar v_{\text{F}}\sqrt{\pi\eta|V_{\text{g}} - V_0|} \tag{4}$$

where v_{F} is the Fermi velocity of graphene ($v_{\text{F}} = 2.5 \times 10^6$ m/s [35]]) and $\eta = \varepsilon_{\text{r}}\varepsilon_0/de$ is derived from the parallel capacitor model (ε_{r} and d are the permittivity and thickness of SiO_2 isolation layer, respectively). As shown in Figure 4, μ_{c} can shift from 0.2 to 0.6 eV as the applied voltage changes from 0.608 to 5.442 V.
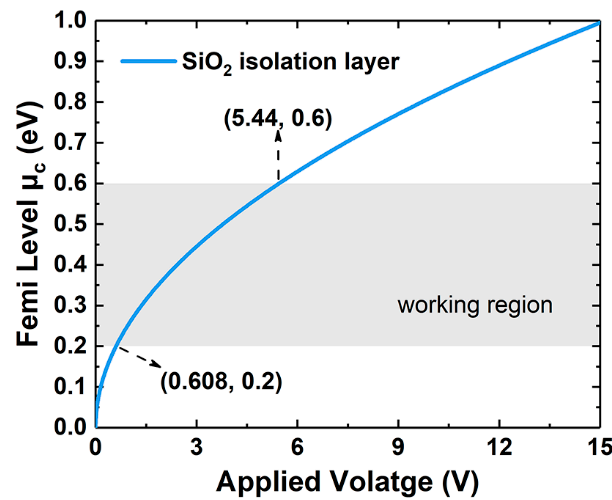
Figure 4. Fermi level μ_c of graphene versus the change of applied external voltage.

3. Design Optimization

To confirm the effect of waveguide dimension on the mode field distribution, the impact of slot width change on the field confinement and metal absorption is investigated, as shown in the Figure 5a–d ($g = h = 50$) and Figure 5e–h ($g = h = 200$ nm), respectively. When g and h increase, the field confinement profiles become slack, which handicap the light–graphene interaction. When a smaller slot width (e.g., 50 nm) is adopted, a higher metal absorption can be expected, since the mode power extends more into the metal layers. When a relatively larger slot width (e.g., 200 nm) is adopted, modes are mainly distributed in SiO$_2$, which implies a relatively lower optical loss. Therefore, systematic dimension analysis is necessary to balance field confinement and metal absorption. In the following geometric discussions, MD is temporarily defined as the difference between MPA ($\mu_c = 1$ eV) and MPA ($\mu_c = 0$ eV), and PL refers to MPA ($\mu_c = 1$ eV) to stress the comparison. The effective index of DBOSW is also calculated at $\mu_c = 0$ and 1 eV. The polarization dependence of proposed design is studied by comparison of N_{eff} at different μ_c and geometric parameters.
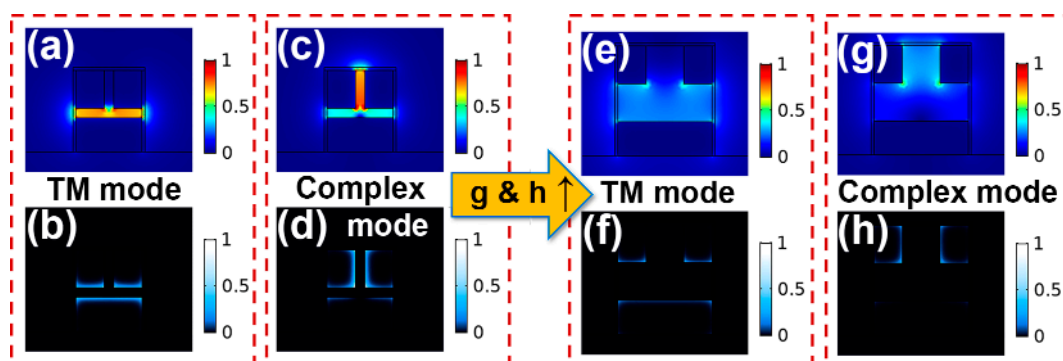

Figure 5. Comparison of normalized electric field distributions and ohmic loss profiles under different waveguide dimensions. When h and g are 50 nm, (**a**,**b**) are electric field distribution and ohmic loss profile for the TM mode, respectively; (**c**,**d**) are corresponding cases for the complex mode. When h and g are 200 nm; (**e**,**f**) are electric field distribution and ohmic loss profile for the TM mode, respectively; (**g**,**h**) are corresponding cases for the complex mode.

3.1. h_b

As mentioned above, the TM mode and complex mode in this hybrid waveguide can be regarded as compound polarizations supported by the vertical, as well as the horizontal Ag-SiO$_2$-Ag structure. The MD, PL and Re(N_{eff}) of the proposed modulator as a function of

bottom Ag slab thickness h_b are shown in the Figure 6. The analysis of h_b is implemented by a similar way adopted in the MIM waveguide model analysis, because it is also with thin metal layers [21]. Compared to complex mode, the TM mode is almost dominated by the longitudinal polarization, therefore the dimension change in vertical direction has a larger impact on the TM mode. Figure 6a shows that $Re(N_{eff})$ of the TM mode is more sensitive to h_b than that of complex mode. The $Re(N_{eff})$ of the TM mode keeps decreasing with the rising of h_b, which decreases from 1.6993 to 1.6464 at $\mu_c = 1$ eV and 1.718 to 1.6654 at $\mu_c = 0$ eV. Meanwhile, $Re(N_{eff})$ of complex mode slowly decreases from $h_b = 50$ nm, and reaches to a stable value at $h_b = 150$ nm. In addition, as shown in Figure 6c, the change in h_b has a significant impact on the PL of the TM mode that decreases with the increasing of h_b and reaches a stable value at $h_b = 150$ nm. In contrast, PL of complex mode remains at around 0.15 dB/µm that is caused by the fraction of the TM mode distributed in the metal layer. This leads to a larger optical loss. The MD change of two modes versus h_b is very small, which is related to the limited influence of h_b on the light field distribution. The $Re(\Delta N_{eff})$ of two modes versus h_b is shown in Figure 6b. Here, $Re(\Delta N_{eff})$ is determined by

$$Re(\Delta N_{eff}) = \left| Re(N_{eff})_{TM\ mode} - Re(N_{eff})_{Complex\ mode} \right| \tag{5}$$

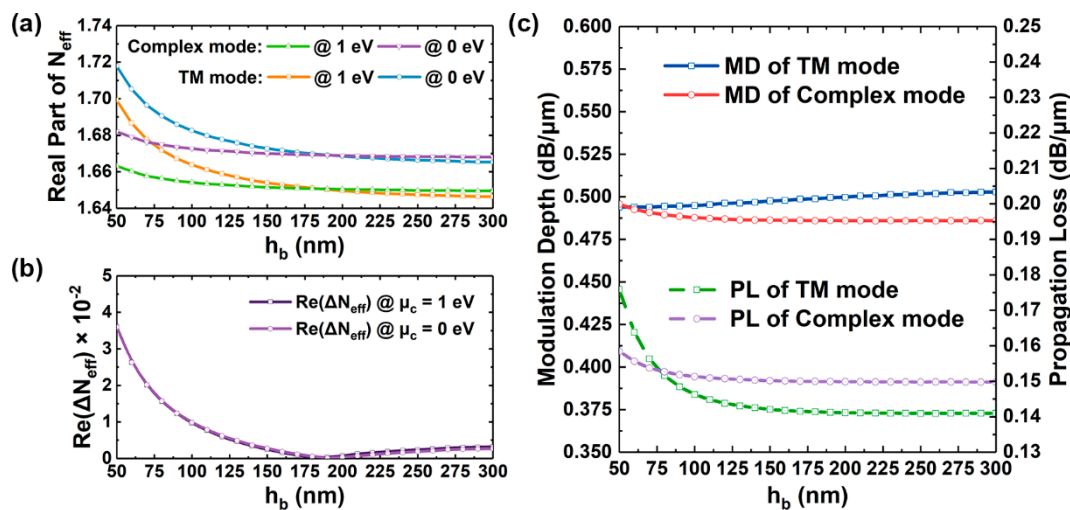**Figure 6.** (**a–c**) are $Re(N_{eff})$, $Re(\Delta N_{eff})$, and modulation depth (MD) as well as propagation loss (PL) of the TM mode and complex mode in the DBOSW modulator as a function of h_b, respectively.

Since a low $Re(\Delta N_{eff})$ is more desirable, h_b is chosen to be 180 nm.

3.2. h

Figure 7 shows the MD, PL, $Re(N_{eff})$ and $Re(\Delta N_{eff})$ of two modes in the DBOSW modulator versus the middle silica layer thickness h. As shown Figure 7a, $Re(N_{eff})$ of both modes reduce consistently with the increasing of h. Furthermore, when $h = 100$ nm, the $Re(N_{eff})$ of the TM mode and complex mode show a very close minimum, which can be confirmed in Figure 7b. Though $Re(\Delta N_{eff})$ can already be restrained at a low level (<0.115) when h is 50 or 200 nm, the thickness of silica layer apparently has a more significant impact on the polarization dependence. As shown in Figure 7c, MD and PL of two modes decrease simultaneously with the increasing of h. These trends are attributed to less confinement of the light field in the middle silica layer as well as the weakening of the interaction with graphene. This is depicted in the illustration in Figure 7c. As h decreases, the electric field intensity of the TM mode and the y-axis electric field component of complex mode increases in the middle silica layer. The increment of mode power in the metal layer invites higher optical loss. To be noted, the MD difference between the TM mode and complex

mode remains at a low level when h varies from 50 to 200 nm. However, the PL of the TM mode becomes lower than that of complex mode when h is higher than 95 nm. To constrain the performance difference between the TM mode and complex mode, h is chosen to be 100 nm.
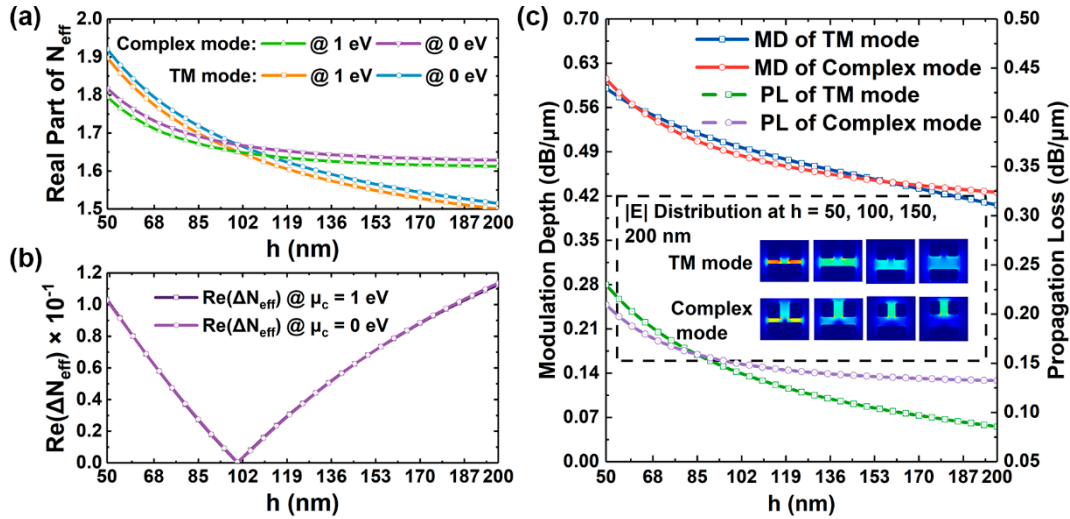

Figure 7. Re(N_{eff}), Re(ΔN_{eff}), MD and PL of the TM mode and complex mode in the DBOSW modulator versus h are shown in (**a**), (**b**) and (**c**), respectively. The illustration in (**c**) shows the variation of electric field distribution for both modes versus h.

3.3. h_t

When $h_b = 180$ nm, $h = 100$ nm, Re(N_{eff}) and Re(ΔN_{eff}), the MD and PL of two modes in the DBOSW modulator versus the top layer thickness h_t are investigated. As shown in Figure 8a, Re(N_{eff}) of the TM mode decreases with the increment of h_t at $\mu_c = 0$ and 1 eV. When h_t is 110 nm, Re(N_{eff}) of the complex mode exhibits a minimum of 1.6722 and 1.6469 at $\mu_c = 0$ and 1 eV, respectively. It is noteworthy that both modes share the same Re(N_{eff}) when h_t is 200 nm and μ_c is 1 eV. This scenario also can be found when h_t is 210 nm and μ_c is 0 eV. In Figure 8b, a maximum Re(ΔN_{eff}) is first presented with the increase of h_t as $\mu_c = 0$ and 1 eV. Then, a minimum Re(ΔN_{eff}) of 6×10^{-4} ($\mu_c = 1$ eV) appears when h_t is 200 nm. A minimum Re(ΔN_{eff}) of 1×10^{-4} ($\mu_c = 0$ eV) can be observed when h_t is 210 nm. The different behaviors of Re(N_{eff}) and Re(ΔN_{eff}) in Figures 8a and 8b can be explained by the change of fringing field distribution as well as the variation in the slot region. This phenomenon is similar to what happens to the MIM waveguide [20]. As shown in Figure 8c, the PLs of both the TM mode and the complex mode decrease till h_t rises up to 200 nm. As h_t increases from 50 nm to 200 nm, the MD of the complex mode decreases by 57.1%, while the MD of the TM mode only reduces by 7.0%. Obviously, the change of h_t has a more remarkable impact on the complex mode than that on the TM mode. This can be explained by the field distribution difference that can be observed from the illustration in Figure 8c. With comprehensive consideration, a balanced h_t of 200 nm is chosen.

3.4. w

For the waveguide structure in Figure 1, the width of the Ag strips w will definitely affect the mode field distribution. Therefore, Re(N_{eff}), Re(ΔN_{eff}), MD and PL of the TM mode and complex mode in the DBOSW modulator versus the Ag strips w are investigated, when $h_b = 180$ nm, $h = 100$ nm, and $h_t = 200$ nm. As shown in Figure 9a, Re(N_{eff}) of the TM mode gradually increases from 1.631 to 1.675 at $\mu_c = 0$ eV, when w varies from 50 to 150 nm. Re(N_{eff}) of the TM mode remains at 1.675, without changing with the increment in w. Inversely, Re(N_{eff}) of complex mode decreases from 1.712 to 1.673 at $\mu_c = 0$ eV, when w

varies from 50 to 150 nm. A negligible change of Re(N_{eff}) of the complex mode is observed when w is over 150 nm. When μ_c = 1 eV, Re(N_{eff}) of the TM mode and complex mode exhibit similar inverse variation with the increment in w, which leads to a turning point of Re(ΔN_{eff}) at w = 150 nm, as shown in Figure 9b.

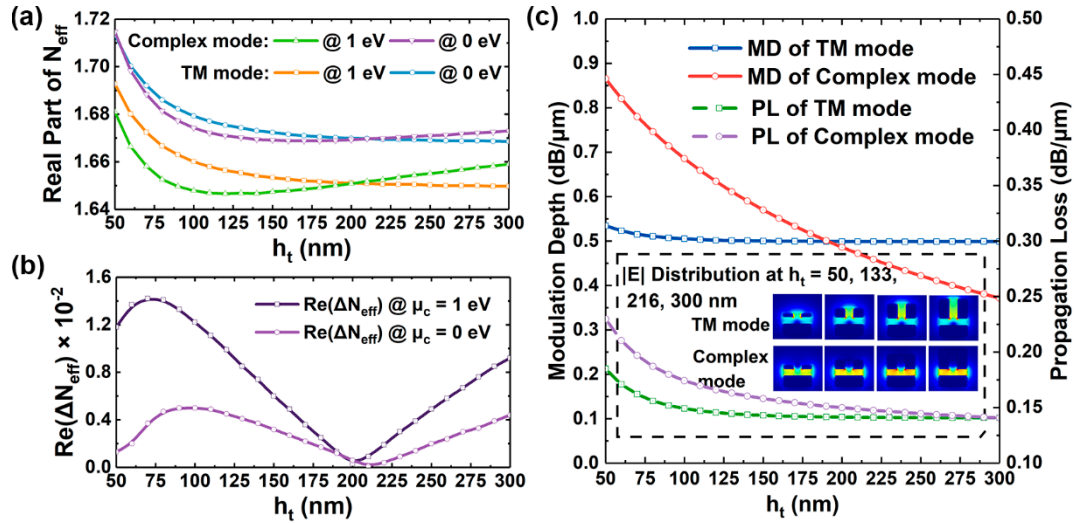**Figure 8.** Re(N_{eff}), Re(ΔN_{eff}), MD as well as PL of the TM mode and complex mode in the DBOSW modulator versus h_t are shown in (**a**), (**b**) and (**c**), respectively. The illustration in (**c**) shows the variation of electric field distribution for the TM mode and complex mode versus h_t.
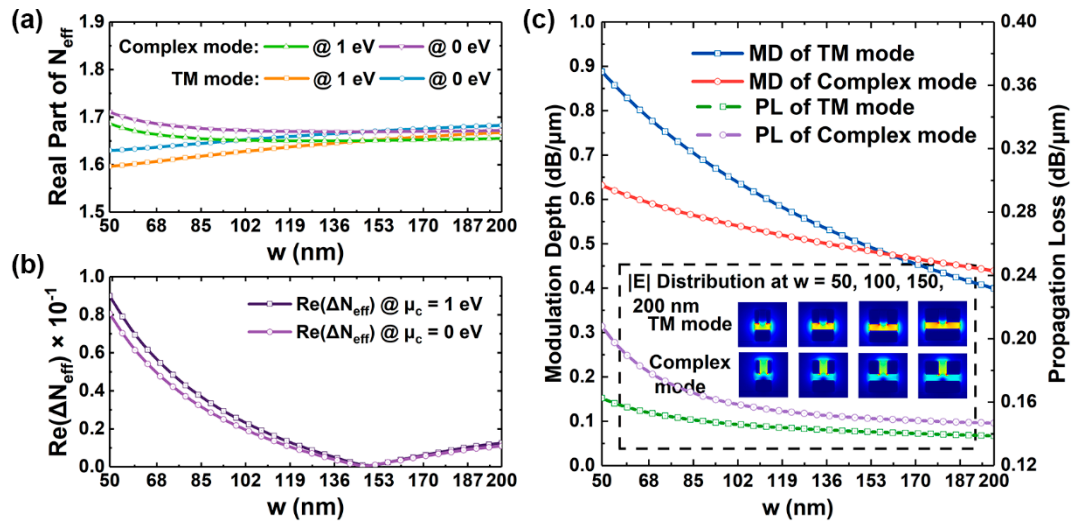

Figure 9. Re(N_{eff}), Re(ΔN_{eff}), modulation depth as well as propagation loss of the TM mode and complex mode in the DBOSW modulator versus w are shown in (**a**), (**b**) and (**c**), respectively. The illustration in (**c**) shows the variation of electric field distribution for both modes versus w.

As w changes from 50 nm to 200 nm, the MDs of the TM mode and complex mode decrease by 55.1 and 30.5%, respectively. Both modes have the same MD at w = 160 nm. When w ranges from 50 to 150 nm, the PL of the TM mode decreases from 0.16 to 0.14 dB/μm, while PL of complex mode from 0.21 to 0.15 dB/μm. Both PLs become stable when w is larger than 150 nm, as shown in Figure 9c. The decrement of the MD and PL can be attributed to the extension of the mode field region with the increment in w, which weakens the graphene–light interaction strength, as shown in the illustration in Figure 9c. Since the TM mode and complex mode are distributed differently in the middle slot and the top

metal slot, the increment in w has a greater impact on the MD of the TM mode. Moreover, the enlargement of the mode field area will weaken the field intensity, and then the metal absorption, leading to a lower PL. From the above, $Re(\Delta N_{eff})$ shows a minimum, while the MDs and PLs of the two modes are very close at w = 150 nm. Therefore, we choose w to be 150 nm in following work.

3.5. g

Another parameter to be confirmed in the proposed design is the gap width g between two upper metal parts. When h_b = 180 nm, h = 100 nm, w = 150 nm and h_t = 200 nm, $Re(N_{eff})$, $Re(\Delta N_{eff})$, MD and PL of the two modes in the DBOSW modulator versus metal slot width g are investigated. As shown in Figure 10, similar variations of $Re(N_{eff})$ and $Re(\Delta N_{eff})$ to that in Figure 9 can be observed.

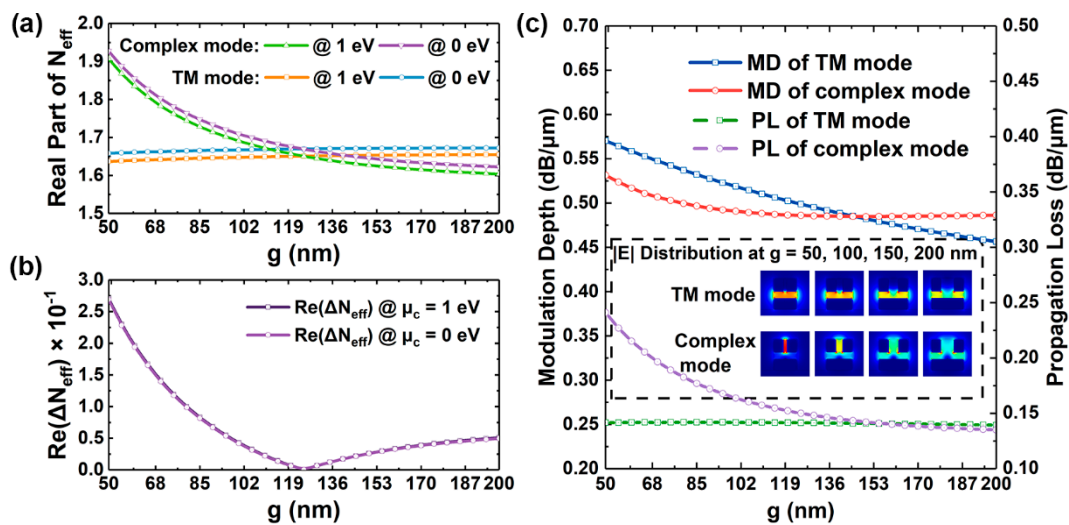**Figure 10.** (**a**–**c**) are $Re(N_{eff})$, $Re(\Delta N_{eff})$, modulation depth as well as propagation loss of the TM mode and complex mode in the DBOSW modulator versus g, respectively; the illustration in (**c**) shows the variation of electric field distribution for both modes versus g.

The difference is that the change of g has a greater impact on $Re(\Delta N_{eff})$ than that on $Re(N_{eff})$. As g increases, $Re(\Delta N_{eff})$ decreases firstly and then gradually increases. At g = 50 nm, $Re(\Delta N_{eff})$ shows the maximum of 0.2707 and 0.2691 for μ_c = 0 and 1 eV, respectively. The minimum $Re(\Delta N_{eff})$ of 6×10^{-4} and 3×10^{-4} can be found at g = 125 nm for μ_c = 0 and 1 eV, respectively.

As shown in Figure 10c, the MD of the complex mode is less sensitive to the variation of g than the TM mode, which is due to the enhanced interaction strength between the x-axis electric field component of complex mode caused by the smaller g and the lateral metal slot. This leads to a higher loss and the resulting lower MD. In contrast, for the TM mode, the variation of g only changes its mode area, which is similar to the impact of w on the TM mode, as shown in the illustration in Figure 10c. The almost unchanged PL and linearly decreasing MD of the TM mode depicted in Figure 10c is consistent with the EA graphene modulator based on the MIM waveguide [36]. Since the difference of MD and PL between the two modes remains at a low level, when g is larger than 125 nm, g is chosen to be 125 nm in this design.

3.6. μ_c Response

The relationships between $Re(N_{eff})$ ($Re(\Delta N_{eff})$), PL, $Im(N_{eff})$ and the chemical potential μ_c also have been investigated. Figure 11a shows that $Re(N_{eff})$ of the TM mode first increases from 1.6699 to the peak value of 1.6772 as μ_c increases from 0 to 0.4 eV. Subsequently, it decreases to 1.6511 as μ_c continues to increase to 1 eV. Similar trends for

$Re(N_{eff})$ of the complex mode can also be observed. Furthermore, the $Re(\Delta N_{eff})$ remains at a low level with an average of 3.6×10^{-4} in the range of $\mu_c = 0$ to 1 eV. Figure 11b shows that the PL decreases rapidly as μ_c decreases from 0.2 to 0.6 eV. Therefore, the "ON" and the "OFF" state of DBOSW modulator is defined at $\mu_c = 0.6$ and 0.2 eV, respectively. In this case, the MD of the TM mode up to 0.474 dB/μm can be obtained, while the MD of the complex mode is 0.462 dB/μm. The calculated ΔMD ($|$MD$_{TM mode} -$ MD$_{Complex mode}|$) is only 0.012 dB/μm at $\lambda = 1550$ nm.
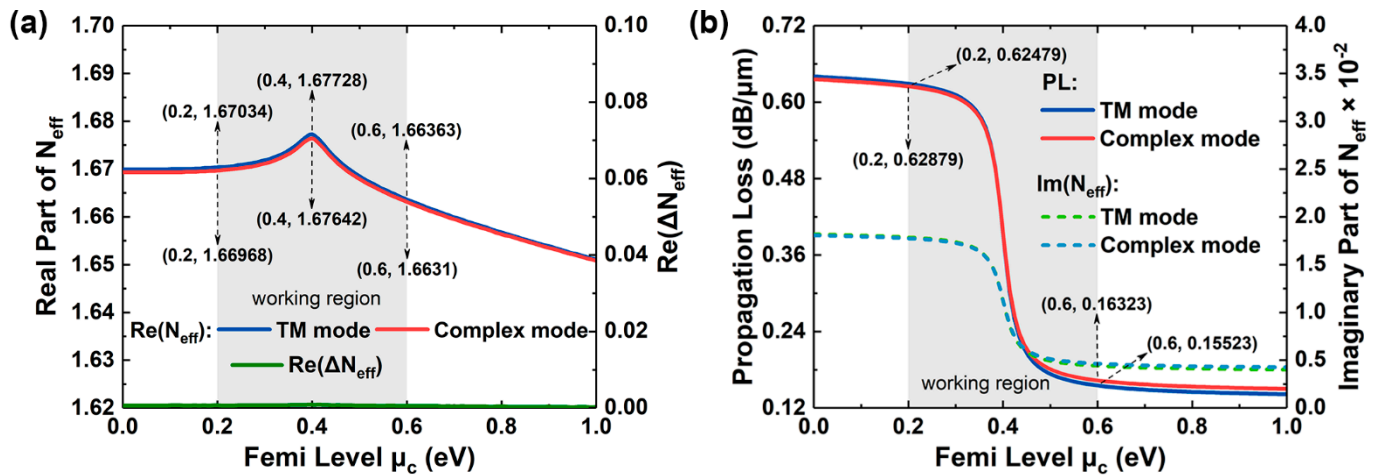
Figure 11. $Re(N_{eff})$ and $Re(\Delta N_{eff})$, $Im(N_{eff})$ and PL of the TM mode and complex mode versus Femi level (chemical potential μ_c) from 0 to 1 eV are shown in (**a**) and (**b**), respectively.

4. Performance and Discussion

4.1. Optical Bandwidth

To confirm the optical bandwidth of the DBOSW modulator with the above geometric parameters, the relationships between $Re(N_{eff})$ and $Re(\Delta N_{eff})$ of the two modes as a function of the incident wavelength are investigated when μ_c ranges from 0.2 to 0.6 eV. As shown in Figure 12a, $Re(N_{eff})$ decreases with the increment in wavelength. When $\lambda = 1.1$ μm and $\mu_c = 0.6$ eV, the maximum $Re(N_{eff})$ of the TM mode and the complex mode is 1.7135 and 1.7163, respectively. When $\lambda = 1.1$ μm and $\mu_c = 0.2$ eV, $Re(N_{eff})$ of the TM mode and complex mode is 1.7096 and 1.7127, respectively. When $\lambda = 1.9$ μm and $\mu_c = 0.6$ eV, $Re(N_{eff})$ of the TM mode and complex mode is 1.6438 and 1.6427, respectively. When $\lambda = 1.9$ μm and $\mu_c = 0.2$ eV, $Re(N_{eff})$ of the TM mode and complex mode is 1.6586 and 1.6574, respectively. It can be observed that a very low $Re(\Delta N_{eff})$ of around 0.001 can be obtained within a wavelength range from 1.1 to 1.9 μm.

In Figure 12b, when the wavelength varies from 1.1 to 1.9 μm, $Im(N_{eff})$ of the TM mode quickly increases from 0.01207 to 0.02164 at $\mu_c = 0.2$ eV; meanwhile, $Im(N_{eff})$ of the complex mode increases from 0.01160 to 0.02177 at $\mu_c = 0.2$ eV, which mainly results from the enhancement of the graphene–light interaction due to the increasing dielectric constant with the increment in optical wavelength. To be mentioned, the MPA change of both two modes is very limited within the wavelength range. The MDs of the TM mode are 0.40918 dB/μm at $\lambda = 1.1$ μm and 0.46931 dB/μm at $\lambda = 1.9$ μm, respectively. While, the MDs of the complex mode are 0.38416 dB/μm at $\lambda = 1.1$ μm and 0.46415 dB/μm at $\lambda = 1.9$ μm, respectively. Therefore, the proposed modulator shows good polarization-independence characteristics over a broad optical bandwidth.
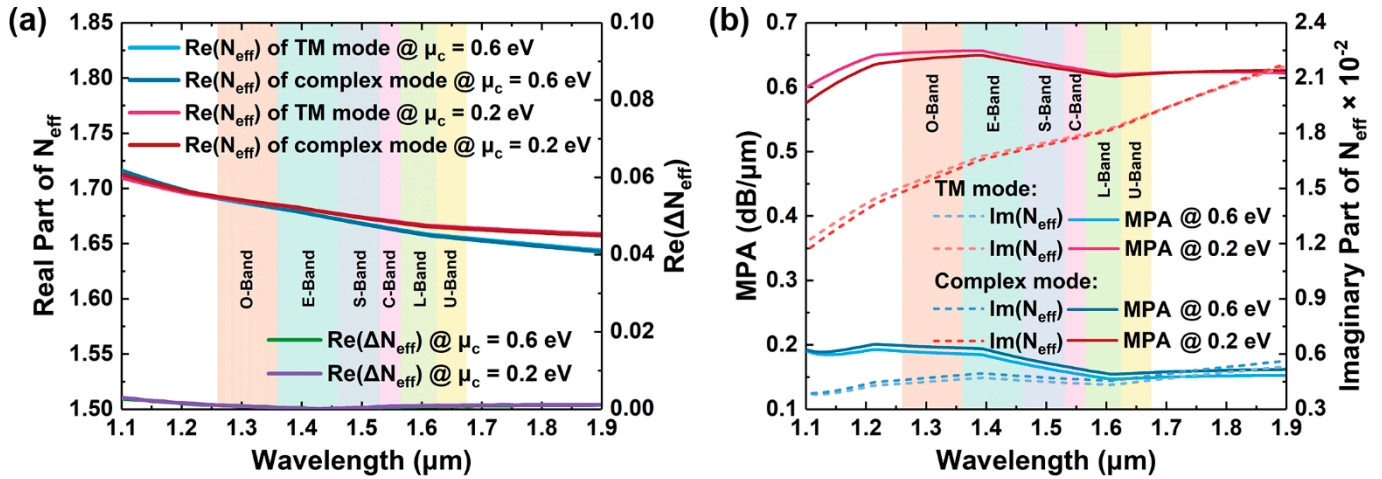
Figure 12. (**a**) $Re(N_{eff})$ and $Re(\Delta N_{eff})$, (**b**) $Im(N_{eff})$ and MPA of the TM mode and complex mode versus the incident wavelength at μ_c = 0.2 and 0.6 eV, respectively.

4.2. Frequency Response

Here, the 3 dB-bandwidth (f_{3dB}) and power consumption of the proposed DBOSW modulator with optimized geometric parameters are also confirmed. An equivalent circuit model is adopted to estimate the dynamic response of the DBOSW modulator, which is shown in Figure 13.
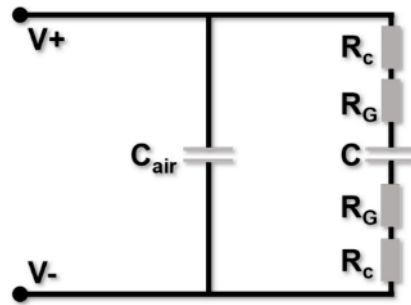

Figure 13. The equivalent circuit model.

In this model, the capacitance C_{air} exists between two electrodes and the air, which is 12 fF [37]. The capacitance C that consists of the two graphene layers and SiO$_2$ isolation layer includes both the dielectric capacitance C_D and the quantum capacitor C_Q. Assuming the graphene layer is undoped (n_s = 0), then we have C_Q = 0. Hence, the capacitance C can be described by the following capacitor model:

$$C = \varepsilon_r \varepsilon_0 w_{ol} L / d \tag{6}$$

where L = 20 µm and w_{ol} = 1385 nm are the graphene modulation length and the overlap width of two graphene layers, respectively. ε_r and d are the permittivity and the thickness of SiO$_2$ isolation layer, respectively. R_{total} is the total resistance, which includes the graphene sheet resistance R_s of 100 Ω/□ [38], and the metal electrode contact resistance to graphene layer R_c of 150 Ω-µm [20]. According to Equation (6) below, R_{total} is calculated to be about 33.85 Ω [24,30], where the effective graphene width w_g is set to be 1.885 µm.

$$R_{total} = 2R_s \times \frac{w_g}{L} + \frac{2R_c}{L} \tag{7}$$

Based on Equation (8), the 3 dB-bandwidth is dominantly limited by *RC* delay. According to Equations (5)–(7), the DBOSW modulator shows a high f_{3dB} of 101 GHz. For the proposed device structure, the silica as an isolation layer that is with a relatively low permittivity and a small thickness of 15 nm is favorable to compensate the disadvantages of the large effective width and overlapping area of graphene layers. In addition, the sheet resistance Rs and contact resistance R_c are values adopted in related Ref. [17].

$$f_{3dB} = \frac{1}{2\pi R_{total} C_{total}} \tag{8}$$

The power consumption ($E_{bit} = C_{total}(\Delta U)^2/4$) is estimated to be 0.271 pJ/bit at L = 20 μm, where the applied voltage change ΔU is 4.834 V. This is in accordance with the change of chemical potential from 0.2 to 0.6 eV.

To clarify the merits of proposed design, the theoretical performance of the reported polarization-insensitive graphene modulators is comprehensively compared with that of this work. As shown in Table 1, the proposed modulator has the largest optical bandwidth and the smallest Re(ΔN_{eff}). Moderate MD and ΔMD also can be obtained. The characteristics of f_{3dB} and Ebit are also better than most reported works.

Table 1. Performance comparison with reported polarization-insensitive graphene modulators at λ = 1.55 μm.

Ref.	Bandwidth (nm)	Re(ΔN_{eff})	MD (dB/μm)	ΔMD (dB/μm)	f_{3dB} (GHz)	E_{bit} (fJ/bit)
[39]	1500–1600	-	0.06	0	13.4	-
[40]	1500–1600	-	0.08	0	80	-
[41]	1200–1600	-	mode A: 1.05, mode B: 1.13, mode C: 0.52	Min: 0.08 Max: 0.61	95	138.8
[42]	1530–1565	4.7×10^{-3}	TM mode: ~0.2975, TE mode: ~0.2895	$\sim 8 \times 10^{-3}$	30.2	2980
[43]	1367–1771	~0.5	TM mode: 1.113, TE mode: 1.119	$\sim 6 \times 10^{-3}$	6.1	7800
[44]	1450–1650	~0.1	TM mode: 1.392, TE mode: 1.347	0.045	~100	-
[45]	1300–1800	1.2×10^{-3}	-	-	135.6	-
This work	1100–1900	6×10^{-4}	TM mode: 0.474, complex mode: 0.462	0.012	101	271

The proposed DBOSW modulator can be implemented through the following fabrication process. The fabrication process starts with a commercial silica wafer. The E-beam evaporation deposits a silver layer with a thickness of 180 nm (h_b) onto the silica surface, serving as a bottom layer. Subsequently, the plasma-enhanced chemical vapor deposition (PECVD) can be used to deposit the 100 nm-thick SiO_2 (h) middle layer. Next, the thermal evaporation is used to deposit a 200 nm-thick (h_t) silver layer followed by electron-beam lithography (EBL) and inductively coupled plasma etching. The 125 nm-wide metal slot substructure (g) is then filled with SiO_2 by PECVD. The subsequent surface chemical mechanical polishing as well as the etching to three layers above can form a hybrid ridge with a width of 425 nm ($w \times 2 + g$). After that, the bottom graphene sheet grown can be wet-transferred to the hybrid ridge waveguide. The graphene-covered region can be defined by EBL processing to remove the excess graphene. Whereas, the graphene on the other side extends 500 nm to form an electrode contact. A 15 nm-thick SiO_2 isolation layer is deposited on the bottom graphene flake. The second graphene flake is transferred onto the SiO_2 isolation layer and handled with the same process applied on the bottom graphene layer, constructing a complete hybrid waveguide structure.

Considering the structural complexity of the proposed DBOSW, the influence of manufacturing errors on the modulator is also evaluated. Firstly, the influence of inequality of the top Ag strip δ (the asymmetry of DBOSW) on the modulator performance is investigated, as shown in Figure 14. The geometric parameters used here are the optimal values discussed in above sections. It can be seen that the DBOSW modulator exhibits stable polarization insensitivity in the fluctuation of one side w from 135 to 165 nm (-15 nm $> \delta > 15$ nm). The maximum Re(ΔN_{eff}) at $\delta = 15$ nm is 4×10^{-3}, which is still lower than the optimal value in Ref. [40]. ΔMD remains at a low level, which is still competitive compared with reported works. The undulation of ΔMD relates to the difference between the mutative MD of the TM mode and the relatively constant MD of the complex mode, as shown in Figure 14c. PLs exhibit good stability. As discussed in Section 3, though the proposed design has a relatively large fabrication tolerance, g needs to be treated carefully. A significant negative effect on Re(N_{eff}) may damage the modulation performance at small g.

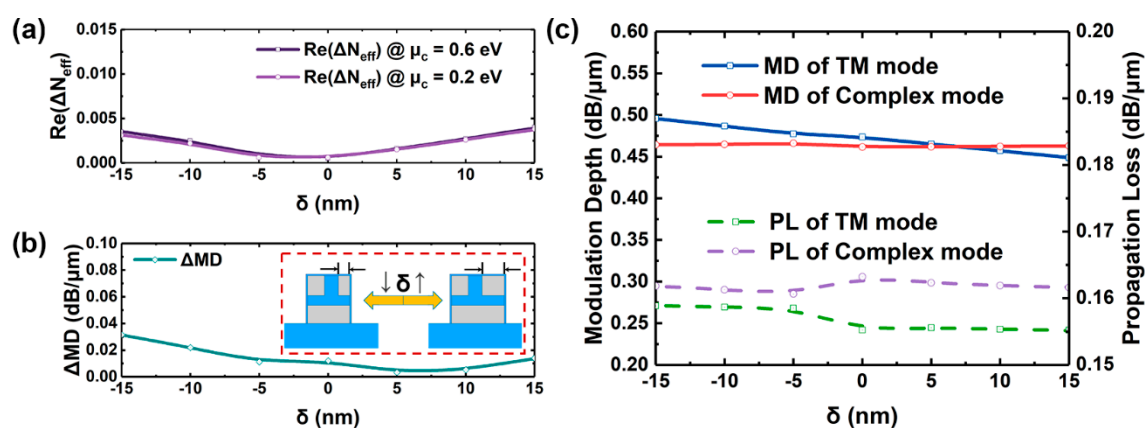**Figure 14.** The inequality of the top Ag strip δ on (**a**) Re(ΔN_{eff}); (**b**) ΔMD; and (**c**) MD, PL of the TM mode and complex mode. The illustration in (**b**) shows the unequal condition of the DBOSW modulator, when $\delta < 0$ the width of the right Ag stripe is smaller than that of the left one.

5. Conclusions

In summary, to achieve the polarization-insensitive modulation and enhance the modulation capability of the graphene layer, a broadband polarization-insensitive graphene modulator based on plasmonic effect with DBOSW is proposed and comprehensively investigated. By introducing the two slot-like structure in the waveguide, the DBOSW can support two modes simultaneously, which enables the modulation of both the longitudinal and the transverse polarization electric fields in a broadband bandwidth. When the external bias voltage shifts from 0.608 to 5.442 V, the MD of 0.474 and 0.462 dB/µm for the TM mode and complex mode can be obtained, respectively. A low effective index difference with an average of 0.001 is achieved within a wide optical band range from 1.1 to 1.9 µm. The 3 dB-bandwidth of 101 GHz and a power consumption of 0.271 pJ/bit at a modulation length of 20 µm can be obtained. The proposed graphene modulator has potential in microwave photonic systems.

Author Contributions: W.C. proposed the idea, carried out the simulations and wrote the manuscript. Y.X. and Y.G. plotted the figures and provided suggestions. X.W. supervised the simulations. X.S. and D.Z. supervised the whole work, interpreted the results and improved the manuscript. All authors reviewed the manuscript. All authors have read and agreed to the published version of the manuscript.

Institutional Review Board Statement: Not applicable.

Informed Consent Statement: Not applicable.

Conflicts of Interest: The authors declare no conflict of interest.

References

1. Marris-Morini, D.; Lyan, P.; Rivallin, P.; Halbwax, M.; Laval, S.; Vivien, L.; Rasigade, G.; Fedeli, J.-M.; Cassan, E.; Le Roux, X.; et al. Recent Progress in High-Speed Silicon-Based Optical Modulators. *Proc. IEEE* **2009**, *97*, 1199–1215. [CrossRef]
2. Wang, C.; Zhang, M.; Chen, X.; Bertrand, M.; Shams-Ansari, A.; Chandrasekhar, S.; Winzer, P.; Lončar, M. Integrated lithium niobate electro-optic modulators operating at CMOS-compatible voltages. *Nature* **2018**, *562*, 101–104. [CrossRef] [PubMed]
3. Pérez-Galacho, D.; Marris-Morini, D.; Stoffer, R.; Cassan, E.; Vivien, L. Simplified modeling and optimization of silicon modulators based on free-carrier plasma dispersion effect. *Opt. Express* **2016**, *24*, 26332–26337. [CrossRef]
4. Park, J.-K.; Takagi, S.; Takenaka, M. InGaAsP Mach–Zehnder interferometer optical modulator monolithically integrated with InGaAs driver MOSFET on a III-V CMOS photonics platform. *Opt. Express* **2018**, *26*, 4842–4852. [CrossRef]
5. Nickelson, L.; Gric, T.; Asmontas, S.; Martavicius, R. Electric Field Distributions of the Fast and Slow Modes Propagated in the Open Rod SiC Waveguide. *Elektron. Elektrotech.* **2009**, *93*, 87–90.
6. Hu, Y.; Pantouvaki, M.; Van Campenhout, J.; Brems, S.; Asselberghs, I.; Huyghebaert, C.; Absil, P.; Van Thourhout, D. Broadband 10 Gb/s operation of graphene electro-absorption modulator on silicon. *Laser Photon. Rev.* **2016**, *10*, 307–316. [CrossRef]
7. Mohsin, M.; Schall, D.; Otto, M.; Noculak, A.; Neumaier, D.; Kurz, H. Graphene based low insertion loss electro-absorption modulator on SOI waveguide. *Opt. Express* **2014**, *22*, 15292–15297. [CrossRef]
8. Dalir, H.; Xia, Y.; Wang, Y.; Zhang, X. Athermal Broadband Graphene Optical Modulator with 35 GHz Speed. *ACS Photonics* **2016**, *3*, 1564–1568. [CrossRef]
9. Phatak, A.; Cheng, Z.Z.; Qin, C.Y.; Goda, K. Design of electro-optic modulators based on graphene-on-silicon slot waveguides. *Opt. Lett.* **2016**, *41*, 2501–2504. [CrossRef] [PubMed]
10. Liu, M.; Yin, X.; Ulin-Avila, E.; Geng, B.; Zentgraf, T.; Ju, L.; Wang, F.; Zhang, X. A graphene-based broadband optical modulator. *Nature* **2011**, *474*, 64–67. [CrossRef]
11. Liu, M.; Yin, X.; Zhang, X. Double-Layer Graphene Optical Modulator. *Nano Lett.* **2012**, *12*, 1482–1485. [CrossRef]
12. Phare, C.T.; Daniel Lee, Y.-H.; Cardenas, J.; Lipson, M. Graphene electro-optic modulator with 30 GHz bandwidth. *Nat. Photonics* **2015**, *9*, 511–514. [CrossRef]
13. Schuller, J.A.; Barnard, E.S.; Cai, W.; Jun, Y.C.; White, J.S.; Brongersma, M.L. Plasmonics for extreme light concentration and manipulation. *Nat. Mater.* **2010**, *9*, 193–204. [CrossRef]
14. Bozhevolnyi, S.I.; Volkov, V.S.; Devaux, E.; Laluet, J.Y.; Ebbesen, T.W. Channel plasmon subwavelength waveguide components including interferometers and ring resonators. *Nature* **2006**, *440*, 508–511. [CrossRef] [PubMed]
15. Gramotnev, D.K.; Bozhevolnyi, S.I. Plasmonics beyond the diffraction limit. *Nat. Photonics* **2010**, *4*, 83–91. [CrossRef]
16. Huang, B.-H.; Lu, W.-B.; Li, X.-B.; Wang, J.; Liu, Z.-G. Waveguide-coupled hybrid plasmonic modulator based on graphene. *Appl. Optics* **2016**, *55*, 5598–5602. [CrossRef] [PubMed]
17. Zheng, P.; Yang, H.; Fan, M.; Hu, G.; Zhang, R.; Yun, B.; Cui, Y. A Hybrid Plasmonic Modulator Based on Graphene on Channel Plasmonic Polariton Waveguide. *Plasmonics* **2018**, *13*, 2029–2035. [CrossRef]
18. Bao, Q.; Zhang, H.; Wang, B.; Ni, Z.; Lim, C.H.Y.X.; Wang, Y.; Tang, D.Y.; Loh, K.P. Broadband graphene polarizer. *Nat. Photonics* **2011**, *5*, 411–415. [CrossRef]
19. Chang, L.-M.; Liu, L.; Gong, Y.-H.; Tan, M.-Q.; Yu, Y.-D.; Li, Z.-Y. Polarization-independent directional coupler and polarization beam splitter based on asymmetric cross-slot waveguides. *Appl. Optics* **2018**, *57*, 678–683. [CrossRef]
20. Zhong, H.; Zhang, Z.Y.; Chen, B.Y.; Xu, H.T.; Yu, D.M.; Huang, L.; Peng, L.M. Realization of low contact resistance close to theoretical limit in graphene transistors. *Nano Res.* **2015**, *8*, 1669–1679. [CrossRef]
21. Veronis, G.; Fan, S. Modes of Subwavelength Plasmonic Slot Waveguides. *J. Lightwave Technol.* **2007**, *25*, 2511–2521. [CrossRef]
22. Geim, A.K.; Novoselov, K.S. The rise of graphene. *Nat. Mater.* **2009**, *6*, 183–191. [CrossRef]
23. Schwierz, F. Graphene transistors. *Nat. Nanotechnol.* **2010**, *5*, 487–496. [CrossRef] [PubMed]
24. Bonaccorso, F.; Hasan, T.; Sun, Z.; Ferrari, A.C. Graphene photonics and optoelectronics. *Nat. Photonics* **2010**, *4*, 611–622. [CrossRef]
25. Kusuma, J.; Balakrishna, R.G.; Patil, S.; Jyothi, M.S.; Chandan, H.R.; Shwetharani, R. Exploration of graphene oxide nanoribbons as excellent electron conducting network for third generation solar cells. *Solar Energy Mater. Solar Cells* **2018**, *183*, 211–219. [CrossRef]
26. Avouris, P.; Chen, Z.; Perebeinos, V. Carbon Based Electronics. *Nat. Nanotechnol.* **2007**, *2*, 605–615. [CrossRef] [PubMed]
27. Bolotin, K.I.; Sikes, K.J.; Jiang, Z.; Klima, M.; Fudenberg, G.; Hone, J.; Kim, P.; Stormer, H.L. Ultrahigh electron mobility in suspended graphene. *Solid State Commun.* **2008**, *146*, 351–355. [CrossRef]
28. Nair, R.R.; Blake, P.; Grigorenko, A.N.; Novoselov, K.S.; Booth, T.J.; Stauber, T.; Peres, N.M.R.; Geim, A.K. Fine Structure Constant Defines Visual Transparency of Graphene. *Science* **2008**, *320*, 1308. [CrossRef] [PubMed]
29. Mak, K.F.; Sfeir, M.Y.; Wu, Y.; Lui, C.H.; Misewich, J.A.; Heinz, T.F. Measurement of the Optical Conductivity of Graphene. *Phys. Rev. Lett.* **2008**, *101*, 196405–196408. [CrossRef] [PubMed]

30. Sensale-Rodriguez, B.; Yan, R.; Kelly, M.M.; Fang, T.; Tahy, K.; Hwang, W.S.; Jena, D.; Liu, L.; Xing, H.G. Broadband graphene terahertz modulators enabled by intraband transitions. *Nat. Commun.* **2012**, *3*, 780–786. [CrossRef]

31. Gric, T.; Nickelson, L.; Asmontas, S. Electrodynamical characteristic particularity of open metamaterial square and circular waveguides. *Prog. Electromagn. Res.* **2010**, *109*, 361–379. [CrossRef]

32. Ye, L.; Sui, K.; Zhang, Y.; Liu, Q.H. Broadband optical waveguide modulators based on strongly coupled hybrid graphene and metal nanoribbons for near-infrared applications. *Nanoscale* **2019**, *11*, 3229–3239. [CrossRef] [PubMed]

33. Hanson, G.W. Dyadic Green's functions and guided surface waves for a surface conductivity model of graphene. *J. Appl. Phys.* **2007**, *103*, 064302–064309. [CrossRef]

34. Kwon, M.-S. Discussion of the Epsilon-Near-Zero Effect of Graphene in a Horizontal Slot Waveguide. *IEEE Photonics J.* **2014**, *6*, 1–9. [CrossRef]

35. Hwang, C.; Siegel, D.A.; Mo, S.K.; Regan, W.; Ismach, A.; Zhang, Y.; Zettl, A.; Lanzara, A. Fermi velocity engineering in graphene by substrate modification. *Sci. Rep.* **2012**, *2*, 590–593. [CrossRef]

36. Ding, Y.; Guan, X.; Zhu, X.; Hao, H.; Xiao, S. Effective electro-optic modulation in low-loss graphene-plasmonic slot waveguides. *Nanoscale* **2017**, *9*, 15576–15581. [CrossRef]

37. Hu, Y.; Xiao, X.; Xu, H.; Li, X.; Xiong, K.; Li, Z.; Chu, T.; Yu, Y.; Yu, J. High-speed silicon modulator based on cascaded microring resonators. *Opt. Express* **2012**, *20*, 15079–15085. [CrossRef]

38. Abdollahi Shiramin, L.; Van Thourhout, D. Graphene Modulators and Switches Integrated on Silicon and Silicon Nitride Waveguide. *IEEE J. Sel. Top. Quantum Electron.* **2016**, *23*, 94–100. [CrossRef]

39. Yang, Z.; Lu, R.; Cai, S.; Wang, Y.; Zhang, Y.; Wang, X.; Liu, Y. A CMOS-compatible and polarization-insensitive graphene optical modulator. *Opt. Commun.* **2019**, *450*, 130–135. [CrossRef]

40. Yang, Z.; Lu, R.; Wang, Y.; Cai, S.; Zhang, Y.; Wang, X.; Liu, Y. A fabrication-friendly graphene-based polarization insensitive optical modulator. *Optik* **2019**, *182*, 1093–1098. [CrossRef]

41. Shirdel, M.; Mansouri-Birjandi, M.A. Broadband graphene modulator based on a plus-shaped plasmonic slot waveguide. *Appl. Optics* **2019**, *58*, 8174–8179. [CrossRef]

42. Hu, X.; Wang, J. Design of graphene-based polarization-insensitive optical modulator. *Nanophotonics* **2018**, *7*, 651–658. [CrossRef]

43. Xu, Y.; Li, F.; Kang, Z.; Huang, D.; Zhang, X.; Tam, H.-Y.; Wai, P. Hybrid Graphene-Silicon Based Polarization-Insensitive Electro-Absorption Modulator with High-Modulation Efficiency and Ultra-Broad Bandwidth. *Nanomaterials* **2019**, *9*, 157–171. [CrossRef] [PubMed]

44. Ye, S.W.; Liang, D.; Lu, R.-G.; Shah, M.K.; Zou, X.-H.; Yang, F.; Yuan, F.; Liu, Y. Polarization Independent Modulator by Partly Tilted Graphene Induced Electro-Absorption Effect. *IEEE Photonics Technol. Lett.* **2016**, *29*, 23–26. [CrossRef]

45. Zou, X.H.; Zhang, Y.J.; Li, Z.H.; Yang, Y.W.; Zhang, S.J.; Zhang, Z.Y.; Zhang, Y.L.; Liu, Y. Polarization-Insensitive Phase Modulators Based on an Embedded Silicon-Graphene-Silicon Waveguide. *Appl. Sci.-Basel* **2019**, *9*, 429–436. [CrossRef]